Cloudiness characteristics over Southeast Asia from satellite FY-2C and their comparison to three other cloud data sets

Xia Jin, Tongwen Wu, Laurent Li, Chunxiang Shi

Cloudiness characteristics over Southeast Asia from satellite FY-2C and their comparison to three other cloud data sets

Xia Jin,[1,2] Tongwen Wu,[1] Laurent Li,[1,3] and Chunxiang Shi[4]

Received 7 November 2008; revised 21 April 2009; accepted 5 June 2009; published 11 September 2009.

[1] Fengyun-2C (FY-2C), launched in October 2004, is the first operational geostationary meteorological satellite in China. It can provide 1-h interval cloudiness products with a spatial resolution of 0.04° latitude × 0.04° longitude. The main characteristics of the regional-scale clouds from a 2-year FY-2C data set (from July 2005 to June 2007) are presented, including the spatial distribution and the annual and diurnal cycles of cloudiness. The reliability of FY-2C cloud products over Southeast Asia is investigated through comparisons to cloud cover from the International Satellite Cloud Climatology Project, the Moderate Resolution Imaging Spectroradiometer on board Terra and Aqua satellites, and conventional ground observations. It is shown that the FY-2C cloud mask performs consistently with other cloud mask products over Southeast Asia. In the boreal winter, the whole domain is dry with little cloudiness. More extensive cloudiness can be observed over the Sichuan Basin, in the East China Sea and the South China Sea, along the northwestern border of China, and around the ITCZ in the Southern Hemisphere. In the boreal summer, the summer monsoon is the dominant system for the studied domain, which is generally humid with extensive cloudiness, corresponding to zones of strong convective activities. Results also reveal considerable discrepancies among different cloud products over extended areas of north China and Mongolia. The Sichuan Basin is another region of large discrepancies among the four cloud products. Diurnal cycles of FY-2C cloudiness for the four seasons of a year are analyzed. The diurnal range of cloudiness is generally larger over land than over ocean. Remarkable diurnal variation is found over the Tibetan Plateau, the northern part of the Indian Peninsula, and central Asia where there is generally less precipitation. The peaks of diurnal cycle of cloudiness appear around local noon over the subtropical land, in the morning over the Indian Peninsula, and in the afternoon near the equator.

Citation: Jin, X., T. Wu, L. Li, and C. Shi (2009), Cloudiness characteristics over Southeast Asia from satellite FY-2C and their comparison to three other cloud data sets, *J. Geophys. Res.*, *114*, D17207, doi:10.1029/2008JD011422.

1. Introduction

[2] Clouds play a major role in controlling the Earth's energy and water cycles at both global and regional scales. They have an enormous impact on the Earth's weather and climate, mainly through their interactions with radiation [e.g., *Liou*, 1986; *Ramanathan et al.*, 1989; *Rossow and Lacis*, 1990; *Stephens and Greenwald*, 1991; *Mokhov and Schlesinger*, 1994; *Rossow and Zhang*, 1995; *Pavolonis and Key*, 2003; *Stephens*, 2005; *Dong et al.*, 2006; *Stephens and Kummerow*, 2007; *Mace and Benson*, 2008]. Clouds currently constitute a major challenge in understanding the past evolution of the climate and in projecting future global climate change [*Cox et al.*, 1987; *Cess et al.*, 1989; *Arking*, 1991; *Intergovernmental Panel on Climate Change*, 1995; *Hogan et al.*, 2001]. We have only limited knowledge of cloud dynamics and quantitative effects on atmospheric general circulation at both global and regional scales. The effects of clouds from different observational estimates or model specifications [*Weare*, 2000; *Hahn et al.*, 2001] have some diversity.

[3] Southeast Asia is one of the cloudiest regions in the world [*Klein and Hartmann*, 1993]. Many works explore the spatial distribution and seasonal cycle of clouds over Southeast Asia [e.g., *Y. Li et al.*, 2004; *Wang et al.*, 2004]. A few others have focused on interdecadal variation [*Li et al.*, 2005] and long-term trends of regional cloudiness [*Kaiser*, 1998, 2000; *Endo and Yasunari*, 2006; *Qian et al.*, 2006; *Warren et al.*, 2007]. *Krüger and Grassl* [2004], as well as *Warren et al.* [2007], discussed the causes for this variation. *Wang et al.* [2004] analyzed the effects of cloud-radiation interactions in the evolution of the East Asian summer monsoon. *Li and Gu* [2006] showed that the variation of

[1]National Climate Center, China Meteorological Administration, Beijing, China.
[2]Also at Chinese Academy of Meteorological Sciences, China Meteorological Administration, Beijing, China.
[3]Also at Laboratoire de Météorologie Dynamique, IPSL, UPMC, CNRS, Paris, France.
[4]National Satellite Meteorological Center, China Meteorological Administration, Beijing, China.

0148-0227/09/2008JD011422

Table 1. Characteristics of the Five-Channel Visible and Infrared Spin Scan Radiometer on Board FY-2C Satellite[a]

Channel	Spectral Band (μm)	Resolution at the Subsatellite Point With One West-East Scanning (km)
VIS	0.55–0.90	1.25
IR1	10.30–11.30	5.00
IR2	11.50–12.50	5.00
IR3	3.5–4.0	5.00
WV	6.30–7.60	5.00

[a]VIS, visible; IR, infrared.

cloudiness in eastern China is strongly related to regional atmospheric circulation. *Yu et al.* [2004] demonstrated that the abundant continental stratus generated on the lee side of the Tibetan Plateau can produce extremely strong cloud radiative forcing and exert a large influence on the local energy balance and regional climate variation. They also suggested that more research (both observation and modeling) must be accomplished to fully document and quantify the effects of clouds on the regional climate of East Asia. In addition, the diurnal cycle of clouds have been explored in different ways on a global scale [*Cairns*, 1995; *Bergman and Salby*, 1996] or regional scale [*Wylie and Woolf*, 2002], but none of these studies aimed at Southeast Asia.

[4] Meteorological satellites are the most powerful platforms for cloud detection. Geostationary satellites, in particular, can provide an overview of cloud systems at synoptic scales, which is very useful for weather monitoring and for construction of long-term climatology. The Fengyun-2 (FY-2) series geostationary meteorological satellites, operated by the China Meteorological Administration (CMA), are devoted to monitoring the environment and to preventing meteorological disasters. They also provide valuable data for exploring the climate of Southeast Asia [*Xu et al.*, 2002; *Zhang et al.*, 2006; *Lu et al.*, 2008]. FY-2C is the first operational satellite of the FY-2 series. It was launched in October 2004, and the derived cloud products are available from June 2005. The purpose of the present study is to investigate the behaviors of cloud cover over Southeast Asia, as observed from FY-2C. The reliability of FY-2C products is also examined through comparisons with three other cloud data sets from the International Satellite Cloud Climatology Project (ISCCP), Moderate Resolution Imaging Spectroradiometer (MODIS), and conventional ground observation (GO) derived from the archives of the National Meteorological Center, CMA. Ground observation data set and ISCCP have already been used widely in past studies of clouds over Southeast Asia. In this work, main attention will be on the characteristics of the regional cloud distribution from FY-2C relative to other cloud products. We also want to check whether FY-2C provides results consistent with other estimates of cloud distribution in Southeast Asia.

[5] Section 2 describes the cloud detection algorithms used in FY-2C and gives a simple introduction to other available cloud data sets. In section 3, regional cloud estimates from FY-2C are compared to those from other cloud climatologies. A few diagnostics are designed to highlight the similarities and differences between FY-2C and each of the other products, for a variety of seasonal conditions. Potential strengths and/or shortcomings of FY-2C are also discussed. Conclusions are given in section 4.

2. Data Sources

[6] FY-2 series of geostationary meteorological satellites, operated by the CMA, are devoted to cloud observation in Southeast Asia. FY-2C is the first operational satellite in the FY-2 series. Its geostationary orbit is located over the equator at 105°E, which makes the effective observation domain extend roughly from 60°N to 60°S and 60°E to 155°E. The major payload in FY-2C is a five-channel Visible Infrared Spin Scan Radiometer (VISSR). Visible, infrared and water vapor images of the Earth and its clouds are derived from the VISSR [*Xu et al.*, 2002; *Lu et al.*, 2008]. The characteristics of the VISSR instrument are listed in Table 1. A complete 20° latitude × 20° longitude scan covering the full Earth disk can be accomplished every 30 min by means of combining satellite spin motion (100 rpm from west-east) and step action of the scan mirror (2500 steps from north to south). It takes 25 min to record the picture, 2.5 min for the mirror retrace, and 2.5 min for VISSR stabilization.

[7] FY-2C provides images with high time resolution (48 observations per day in the season of high flooding risk in China and 24 per day in other seasons) with a spatial resolution of 0.04° latitude × 0.04° longitude. To detect whether each pixel is cloudy or not, an algorithm [*Yang et al.*, 2008] similar to that of ISCCP [*Rossow and Garder*, 1993a] is used for satellite IR radiance data collected at channel 1 (i.e., IR1 in Table 1) in FY-2C. The scheme includes six steps:

[8] 1. On the basis of a vegetation map which is produced from the latest available data by the U.S. Geological Survey's EROS (Earth Resources Observation Systems) Data Center, the FY-2C effective observation domain, roughly from 60°N to 60°S and 60°E to 155°E, is divided into 20 latitudinal zones each 5.5° wide. Each zone is then classified into different zones according to elevation above mean sea level (zs): $zs \leq 1000$ m, 1000 m $< zs \leq 2000$ m, 2000 m $< zs \leq 3000$ m, 3000 m $< zs \leq 4000$ m and $zs >$ 4000 m. Each zone is classified into four categories of regions on the basis of surface type, including water bodies and sea, ice, arid and semiarid land, and other land. The cloud detection is done in these individual regions.

[9] 2. Variation in surface brightness temperature ($\Delta T_{surf,1h}$) over 1-h interval can be estimated from the FY-2C satellite IR1 channel radiance for the four categories of surfaces at different times of day. The maximum ($\Delta T^{\max}_{surf,1h}$) of $\Delta T_{surf,1h}$ in artificially selected clear-sky pixels that are roughly recognized by the human's eyes and in different seasons can be estimated. Here only the satellite observation data in all the year of 2006 are used.

[10] 3. The cloudy pixels located at the boundaries of moving clouds and rapidly developing clouds can be detected if 1-h variation of surface brightness temperature $\Delta T_{surf,1h}$ is beyond the range of surface brightness temperature variation $\Delta T^{\max}_{surf,1h}$ for that surface category. The key assumption behind this test is that clouds are generally characterized by lower temperature than the underlying earth surface.

[11] 4. For any pixel in a given time t, its brightness temperature (BT) is defined as BT_t. Over a 15-day running

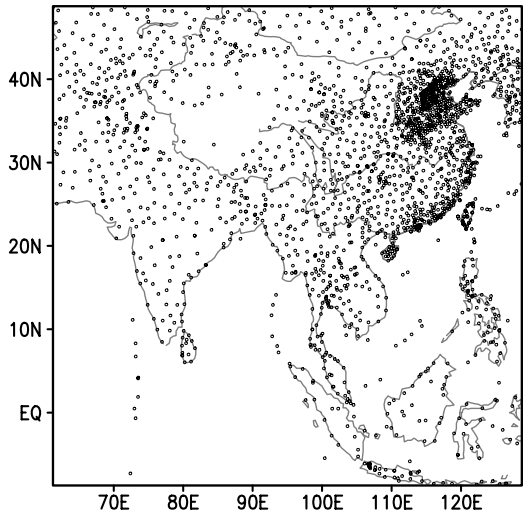

Figure 1. Location of the selected ground observation stations.

interval, spanning 7 days before and 7 days after time t, the maximum of the brightness temperature in the former 7 days ($BT_{t-7}^{\max}$) and the maximum in the latter 7 days ($BT_{t+7}^{\max}$) can be computed. Here the fundamental premise is that each 7-day time period includes more than one clear-sky day at each location. So, $BT_{t-7}^{\max}$ and $BT_{t+7}^{\max}$ can be, separately, regarded as the surface brightness temperatures in each 7-day time period.

[12] 5. Most pixels generally satisfy $|BT_{t-7}^{\max} - BT_{t+7}^{\max}| \leq 10\ K$. The pixel is detected as a cloudy pixel when $BT_{t+7}^{\max} - BT_t > \Delta BT_{crit}$, otherwise it is clear-sky. Here, the threshold ΔBT_{crit} is the sum of the minimum of the brightness temperature biases in between clear-sky and cloudy pixels and the FY-2C measurement error BT_{error}. That is

$$\Delta BT_{crit} = \min\left(BT_{t+7}^{\max} - BT_{t,cb}\right) + BT_{error}, \qquad (1)$$

where $BT_{t,cb}$ are the BT at all the cloudy pixels detected in step 3. BT_{error} is the FY-2C observation error, which was set to 1.0 K for water bodies and ocean, 2.2 K for land, 2.5 K for ice, and 2.5 K for desert.

[13] 6. If there exists $|BT_{t-7}^{\max} - BT_{t+7}^{\max}| > 10\ K$, which means that there is a large seasonal variation of surface temperature, a cloudy pixel is detected only when $BT_{t+7}^{\max} - BT_t > |BT_{t+7}^{\max} - BT_{t-7}^{\max}|$, otherwise it is a clear-sky pixel.

[14] All the pixels can be placed into the clear-sky or cloudy category using the clear-sky background algorithm described above. The present study selected a 2-year period from July 2005 to June 2007. The studied area is 60°E∼130°E, 10°S∼50°N, involving the main Asian monsoon region. To facilitate data treatment, we first calculated cloud cover in a regular grid of 2.5° latitude × 2.5° longitude by considering the proportion of cloudy pixels. Daily values are obtained through a simple average of all available samples of each day. They are further processed to have monthly mean data.

[15] Three data sets were used to evaluate the quality and reliability of FY-2C cloud cover, namely, MODIS, ISCCP and GO. MODIS [*Salomonson et al.*, 1989; *Barnes et al.*, 1998, 2003] is one of the key instruments for the National Aeronautics and Space Administration's (NASA) Earth Observing System (EOS). The sensor has 36 spectral bands with wavelengths ranging from 0.41 to 14.5 μm (20 reflective solar bands from 0.41 to 2.1 μm and 16 thermal emissive bands with wavelengths above 3.7 μm). It is currently operated on board the EOS/Terra and EOS/Aqua satellites, launched in December 1999 and May 2002, respectively. The Terra and Aqua satellites view Earth from Sun-synchronous polar orbits at an altitude of 705 km. The equator-crossing time of Terra is 1030 local time (descending node) while that of Aqua is 1330 local time (ascending node). The MODIS cloud mask is generated twice daily, at 1-km and 250-m (at nadir) spatial resolutions; however, the 250-m cloud mask flags are based on the visible channel data only. A complete description of the MODIS cloud mask products is given by *Ackerman et al.* [1998] and *Menzel et al.* [2008]. In this paper, we used the MODIS level 3 daily products [*Hubanks et al.*, 2008], which span a 24-h (0000 to 2400 UT) interval and summarize the globe at 1° resolution. The data sets from Terra and Aqua are used together to minimize the effect of the diurnal cycle, through averaging both for each day.

[16] The ISCCP [*Rossow and Schiffer*, 1999] is a major international effort to study clouds from operational meteorological satellites. Data were collected from the suite of meteorological satellites operated by several nations, consisting of five geostationary satellites (the Geostationary Meteorological Satellite (GMS), the Geostationary Operational Environmental Satellite (GOES), Meteosat, and the Indian National Satellite (INSAT)) and two polar-orbiting satellites [the Advanced Very High Resolution Radiometer (AVHRR) onboard two different National Oceanic and Atmospheric Administration (NOAA) satellites]. The validation of ISCCP products is given by *Rossow and Garder* [1993b]. Monthly cloud fractions in the ISCCP D2 product at a 280-km resolution equal area map grid are used in this work.

[17] We also use a ground observation data set (hereafter GO) from the synoptic observer reports over Southeast Asia and the western Pacific, archived at the National Meteorological Center, CMA. Cloud cover is estimated visually by trained observers using general rules stipulated by *World Meteorological Organization* [1975, 1987]. Monthly cloud fraction was constructed from the original 6-hourly weather observation reports. After removing a few stations, the records of which were incomplete or of poor quality, 2217 stations (shown in Figure 1) were selected to cover the target area of our work. These data were then merged onto 2.5° latitude × 2.5° longitude cells to facilitate quantitative comparisons with other data.

3. Results

3.1. Mean Cloudiness in Winter and Summer

[18] Spatial distributions of the mean total cloudiness from FY-2C, ISCCP, MODIS, and Ground Observation averaged for boreal winter (December, January and February) are shown in Figure 2. All of the cloud data sets capture the main features of the spatial distribution of cloud in Southeast Asia. We can easily observe an area of high values over the western part of the maritime continent, with maxima above 80%, corresponding to the wet season of this region

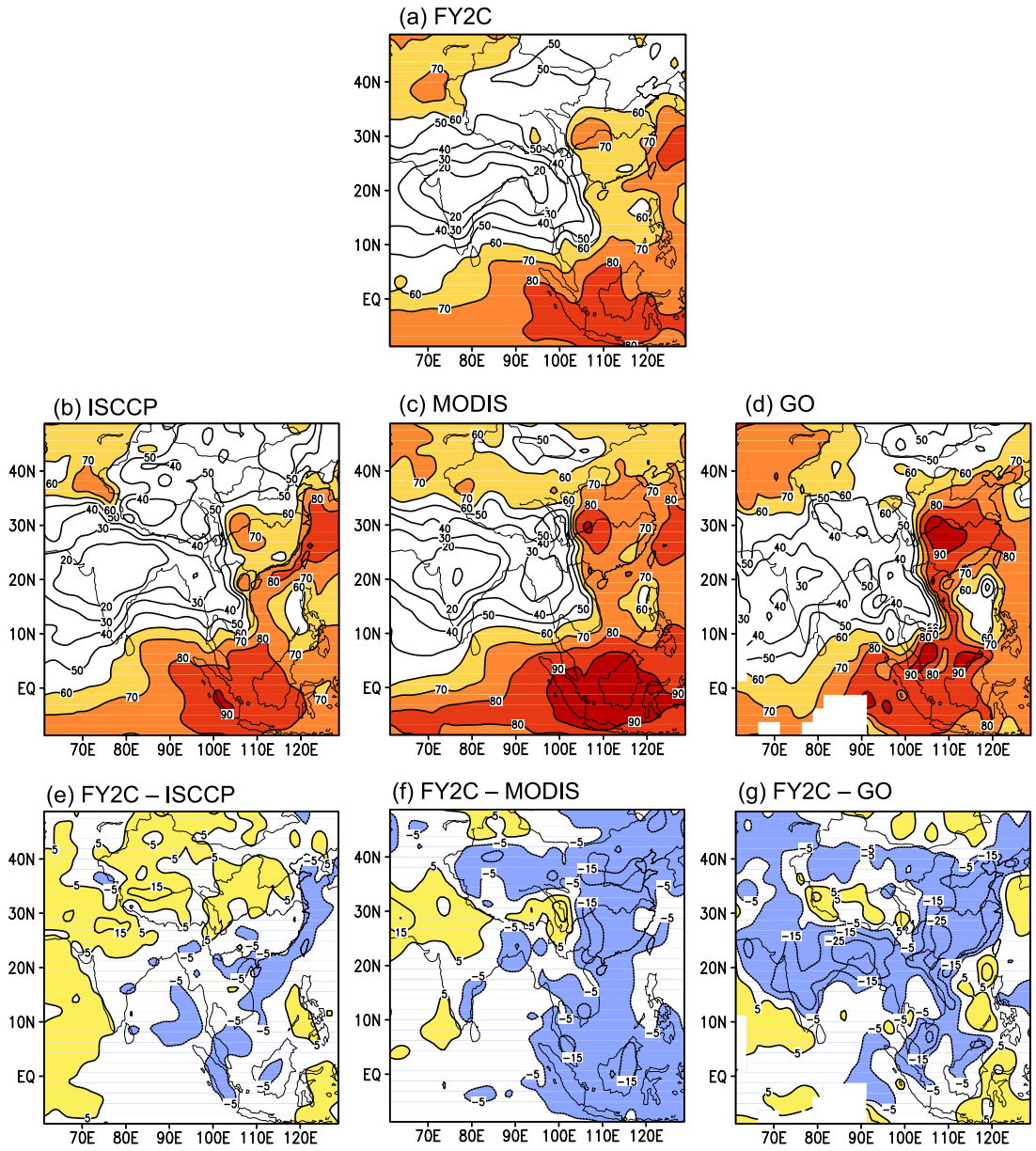

Figure 2. Mean cloudiness of December-January-February for (a) FY-2C, (b) ISCCP, (c) MODIS, and (d) GO. Contour interval is 10% sky cover, and colored areas show cloudiness greater than 60%. Differences between FY-2C and (e) ISCCP, (f) MODIS, and (g) GO. Colored areas show differences greater than 5% sky cover or less than −5%.

with abundant precipitation. Over the Yangtze River Valley, high cloudiness clearly exists and reveals the influence of the topography. The center is located to the east of the Tibetan Plateau, i.e., over the Sichuan Basin. Satellite-based data sets (Figures 2a–2c) clearly show that a region with high cloudiness exists over the East China Sea, with values larger than 80%, and extends to the coasts of the South China Sea. These abundant cloud covers are related to advection of cold continental air masses over much the warmer sea surface, causing instabilities and even explosive storms. Apart from the above mentioned regions, there also exists an area of high cloudiness over central Asia. An area with values larger than 70% can be observed over the Pamir Mountains, which can be attributed to baroclinic instabilities developed with the midlatitude jet stream. For all four data sets, low cloudiness is found for a large region extending from the Arabian Sea to the Indo-China Peninsula. The period of DJF is the dry season for this region, with dry northeasterlies from the Asian continent. There are two centers of low cloudiness, with the lowest amount under 20%. One is located from the middle of the Indian Peninsula to the northeast area of the Arabian Sea, and the other in Myanmar. Low cloudiness is also found in the arid areas in Mongolia and north China.

[19] Large regional discrepancies can, however, be found among the four data sets. Figures 2e–2g present the differences between FY-2C and the three comparison data sets (ISCCP, MODIS, and GO, respectively). Clouds from FY-2C

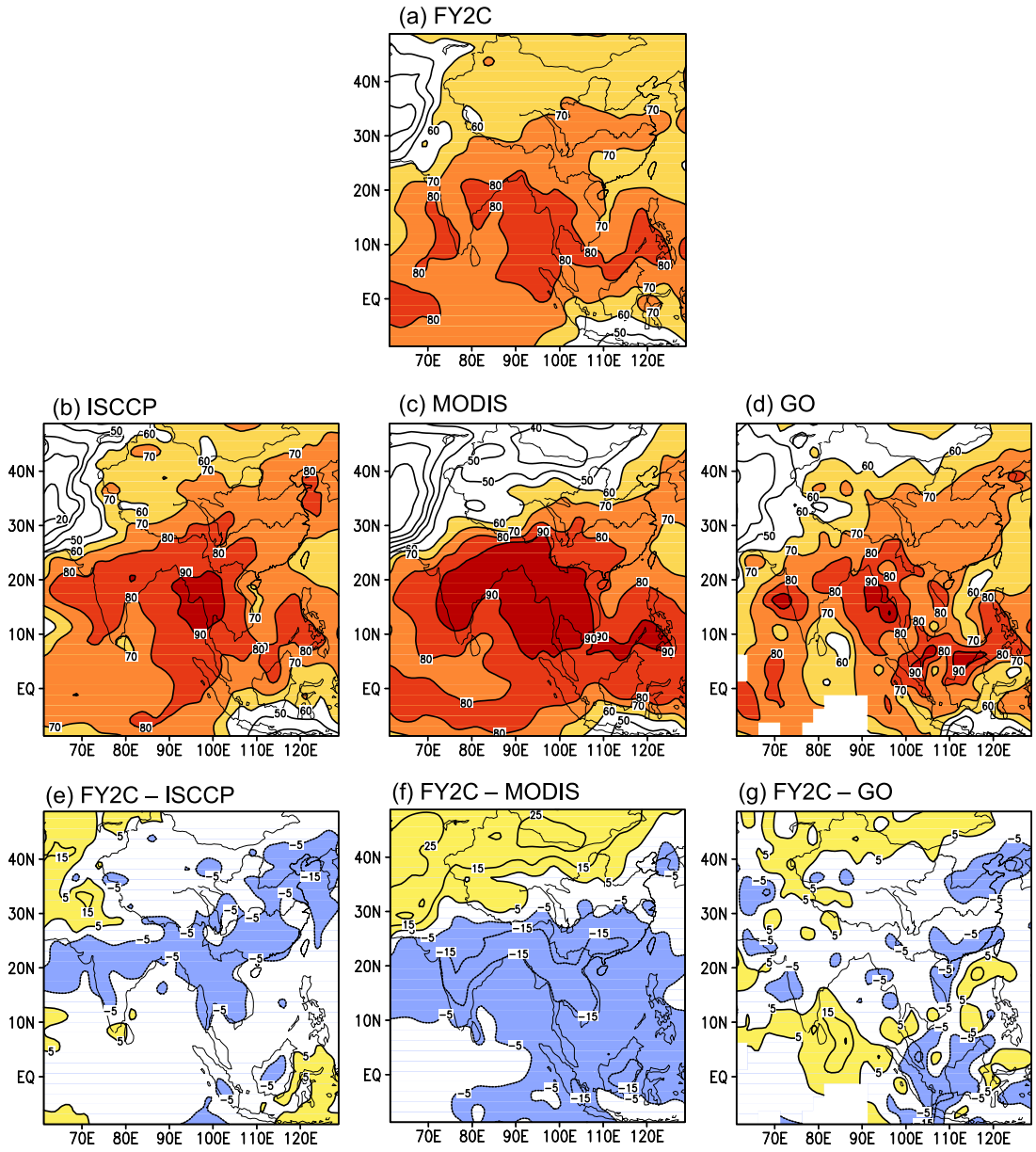

Figure 3. Same as in Figure 2 but for the average of June-July-August.

are close to the ISCCP data. There are only small regions in the western Pacific off the Asian coast where the cloud level from FY-2C is about 10% smaller than that from ISCCP. Compared to MODIS, a large discrepancy is found over the whole western part of the maritime continent, the arid and semiarid region in northwestern and northern China, and southern China, where FY-2C underestimates clouds about 10%. Compared to the ground observations (Figure 2g), the remarkable discrepancy is that the FY-2C cloudiness over the Indian Peninsula, south of the Tibetan Plateau, and over East Asia are about 20% to 30% smaller than the cloudiness in GO. We can, however, note that, compared to the three satellite-derived data sets, cloudiness in GO is generally larger over land but much smaller over water. This is certainly due to the lack of surface observation over seas.

[20] In the boreal summer, as shown in Figure 3, the geographical pattern of the June-July-August (JJA) mean cloudiness from FY-2C resembles that from the three other data sets. All four data sets exhibit abundant cloudiness larger than 70% in the tropics and subtropics in the Northern Hemisphere (0–30°N). Compared to the boreal winter, the main high cloudiness area shifted northward seasonally to the region of 10–20°N during the boreal summer. There are three separate maximum regions: over the southwest of the Indian Peninsula, northeast of the Bay of Bengal, and west of the Philippines. They are all centers of strong precipitation (not shown). As shown in Figure 3a, there is a zone of high cloudiness over central China. It also exists in other data sets. A low-cloudiness area with less than 70% cloudiness mainly covers central Asia (from the Iranian Plateau to Outer Mongolia), around the Jawa Island in Indonesia, and over the subtropical northwest Pacific east to China. All three regions of low cloudiness, where there are little precipitation in the boreal summer (not shown), are

Table 2. Spatial Pattern Correlation Coefficients of the Annual Mean Cloudiness for Each Two-Member Combination of the Four Data Sets: FY-2C, ISCCP, MODIS, and Ground Observation

	ISCCP	MODIS	Ground Observation
FY-2C	0.90	0.82	0.56
ISCCP	–	0.90	0.72
MODIS	–	–	0.74

located in the three anticyclonic systems: the Iranian High, the Australian High and the Northwest Pacific Subtropical High. Over north China, a low-cloudiness zone is over the Gobi Desert and the semiarid region.

[21] Figures 3e–3g show differences between FY-2C and the three other data sets (ISCCP, MODIS, and GO, respectively). Similar to the winter season, in the boreal summer FY-2C is very close to ISCCP. As shown in Figure 3e, in very cloudy regions (with cloudiness greater than 70% in Figure 3b), ISCCP estimates slightly more cloudiness than FY-2C, with less than a 10% difference. Small negative differences are mainly found over regions of smaller cloudiness (less than 70%). Compared to MODIS, the FY-2C estimates about 10% less cloudiness over most areas in the south of 30°N and estimates about 20% more cloudiness in the north of 30°N. As shown in Figure 3g, the differences in cloudiness between FY-2C and GO are almost limited to the range of −10% to 10%. These differences in the boreal summer (Figure 3g) are significantly smaller than those in boreal winter (Figure 2g).

[22] To quantify the relative agreement among the four data sets, we calculated the spatial pattern correlation coefficients for every pair of data sets. The calculation is applied to the mean annual cloudiness in the region from 60°E to 130°E and 10°S to 50°N. However, calculations involving GO are realized at the irregular grid formed by the surface stations. Results shown in Table 2 confirm the high

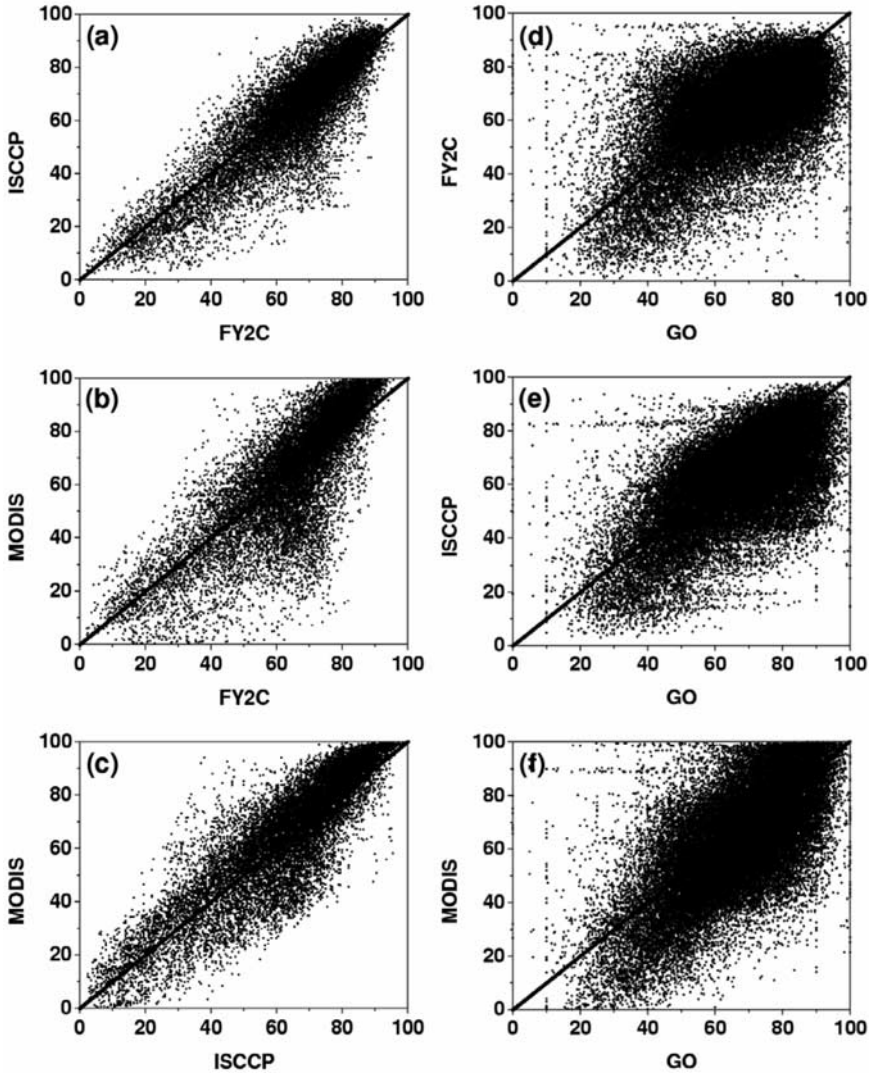

Figure 4. Scatterplots of mean monthly cloudiness in (a) FY-2C versus ISCCP, (b) FY-2C versus MODIS, (c) ISCCP versus MODIS, (d) FY-2C versus GO, (e) ISCCP versus GO, and (f) MODIS versus GO for the period from July 2005 to June 2007. Figures 4a–4c are between individually matched map grid cells. Figures 4d–4f (involving GO) are based on surface stations with a preinterpolation of FY-2C, ISCCP, and MODIS.

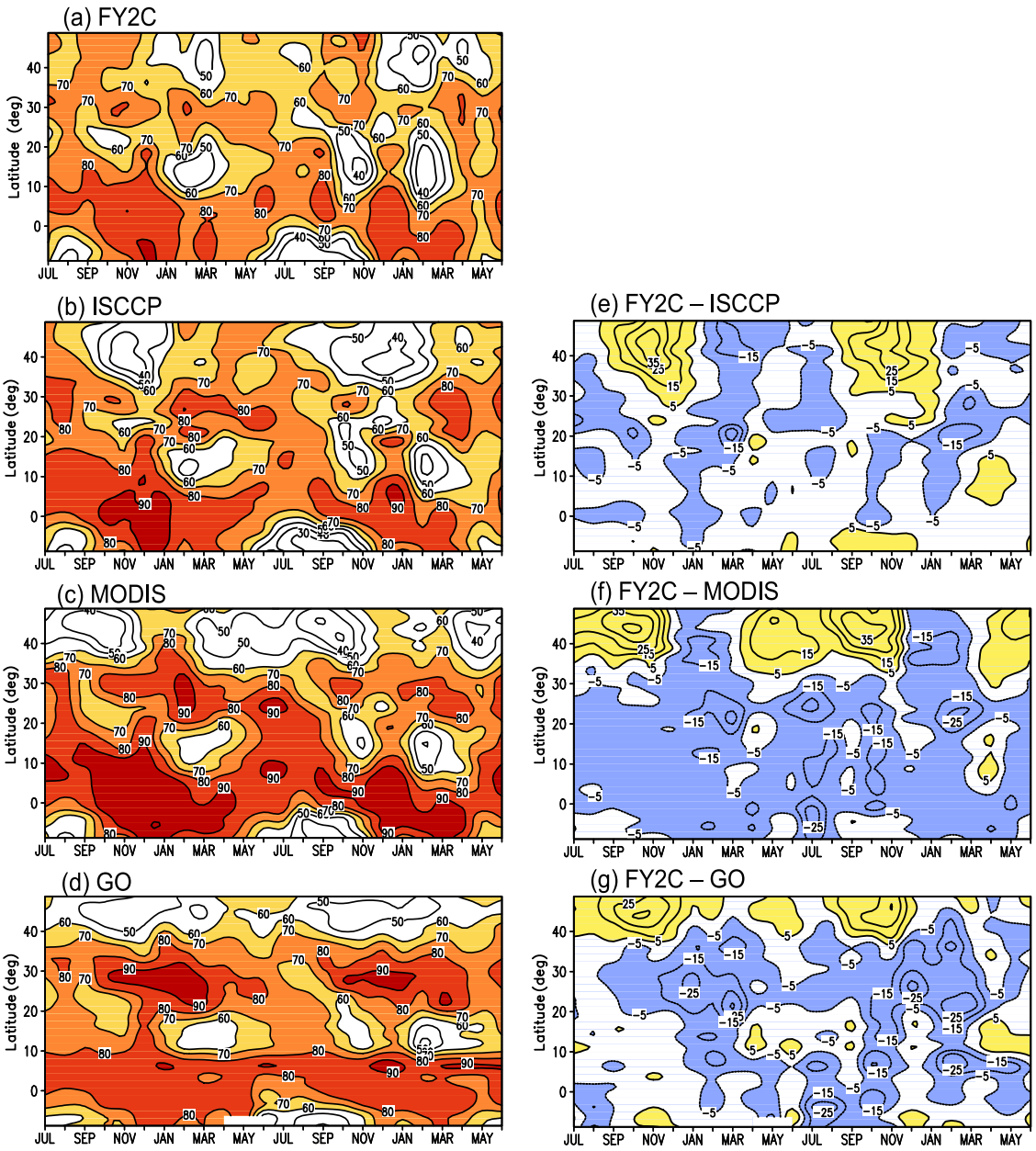

Figure 5. Time-latitude diagrams of monthly mean cloudiness (% sky cover) averaged from 105°E to 115°E for (a) FY-2C, (b) ISCCP, (c) MODIS, and (d) GO. Contour interval is 10%, and colored areas show cloudiness levels greater than 60%. Differences between FY-2C and (e) ISCCP, (f) MODIS, and (g) GO. Colored areas show differences greater than 5% or less than −5%.

consistency among the satellite-derived cloudiness and the correlation coefficients range from 0.82 to 0.90. FY-2C has a higher correlation with ISCCP than with MODIS. Correlation coefficients involving GO are generally lower.

[23] Figure 4 shows scatter diagrams of monthly mean cloudiness from July 2005 to June 2007 for each two-member combination of FY-2C, ISCCP, MODIS and GO. These diagrams are plotted at surface stations, which imply an interpolation from grid points to individual surface stations for the satellite-derived data sets. Some systematic differences among the four data sets can be observed in Figure 4. Compared to ISCCP and MODIS, FY-2C tends to give larger values (Figures 4a and 4b) for cloudiness smaller than 50%, but lower values for cloudiness greater than 80%. Comparison between ISCCP and MODIS (Figure 4c) gives a quite satisfactory result. Figures 4d–4f show diagrams involving GO and each of the satellite data sets. The consistency is generally weaker than that between two satellite-derived data sets. When cloudiness is smaller than 40%, GO seems to estimate higher cloudiness than satellite data do. The reason is probably that a low amount of cloud cover is easily ignored by satellites, but still visible for surface observers.

3.2. Temporal Variation of Cloudiness

[24] Our data sets cover 2 years from July 2005 to June 2007, which allows us to study seasonal variations as well

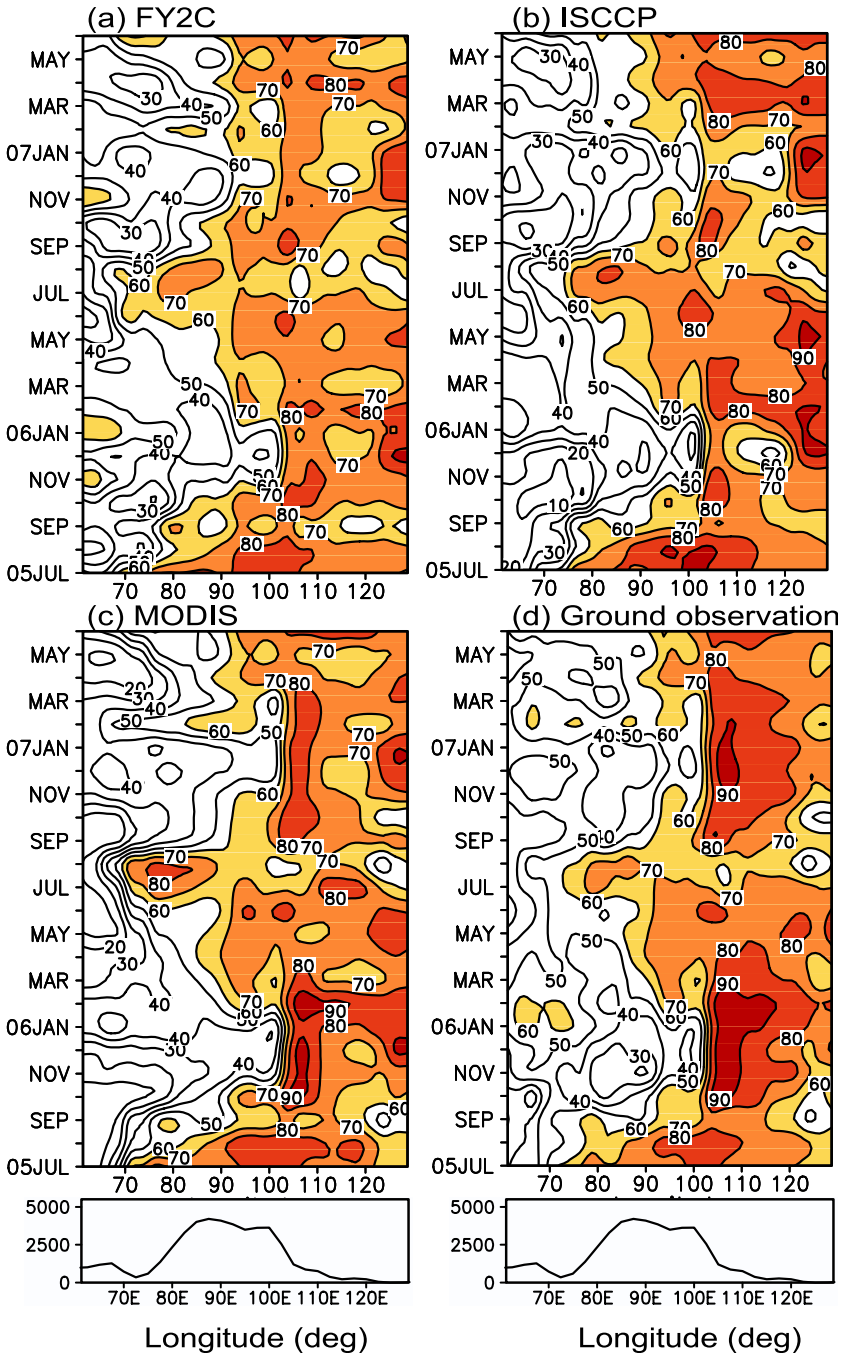

Figure 6. Time-longitude diagrams of monthly mean cloudiness averaged for latitudes from 27.5°N to 32.5°N. Surface topography (m) is sketched at the bottom.

as differences between the two annual cycles. Figure 5 presents the Hovmöller diagrams of mean cloudiness, averaged over the longitudes of 105°E to 115°E, as a function of latitude and time. All four cloud data sets are plotted in Figures 5a–5d. At a first glance, we can recognize two bands of high cloudiness situated around the equator and 30°N, and two bands of low cloudiness situated at 15°N and 45°N. The two bands of high cloudiness correspond to the ITCZ and the Yangtze River valley. The two low-cloudiness bands correspond to the subtropical anticyclonic zone and the semiarid area in north China. Between 10°S and 15°N, we can clearly observe that centers of maximum cloudiness follow the meridional shift of the ITCZ with seasons, and the four data sets (especially the three satellite-based ones) are very consistent. During the period of May to October, the mean latitude of maximum cloudiness shifts from the equatorial sea area to the north continental area, and then backs southward to the sea, corresponding to the shift of the rain belt (not shown). We can also see that cloudiness is generally less abundant in the second annual cycle, from July 2006 to June 2007, than in the first annual cycle, from July 2005 to June 2006. In the subtropics of the Northern Hemisphere (around 15°N), low cloudiness can be observed from October to April, but

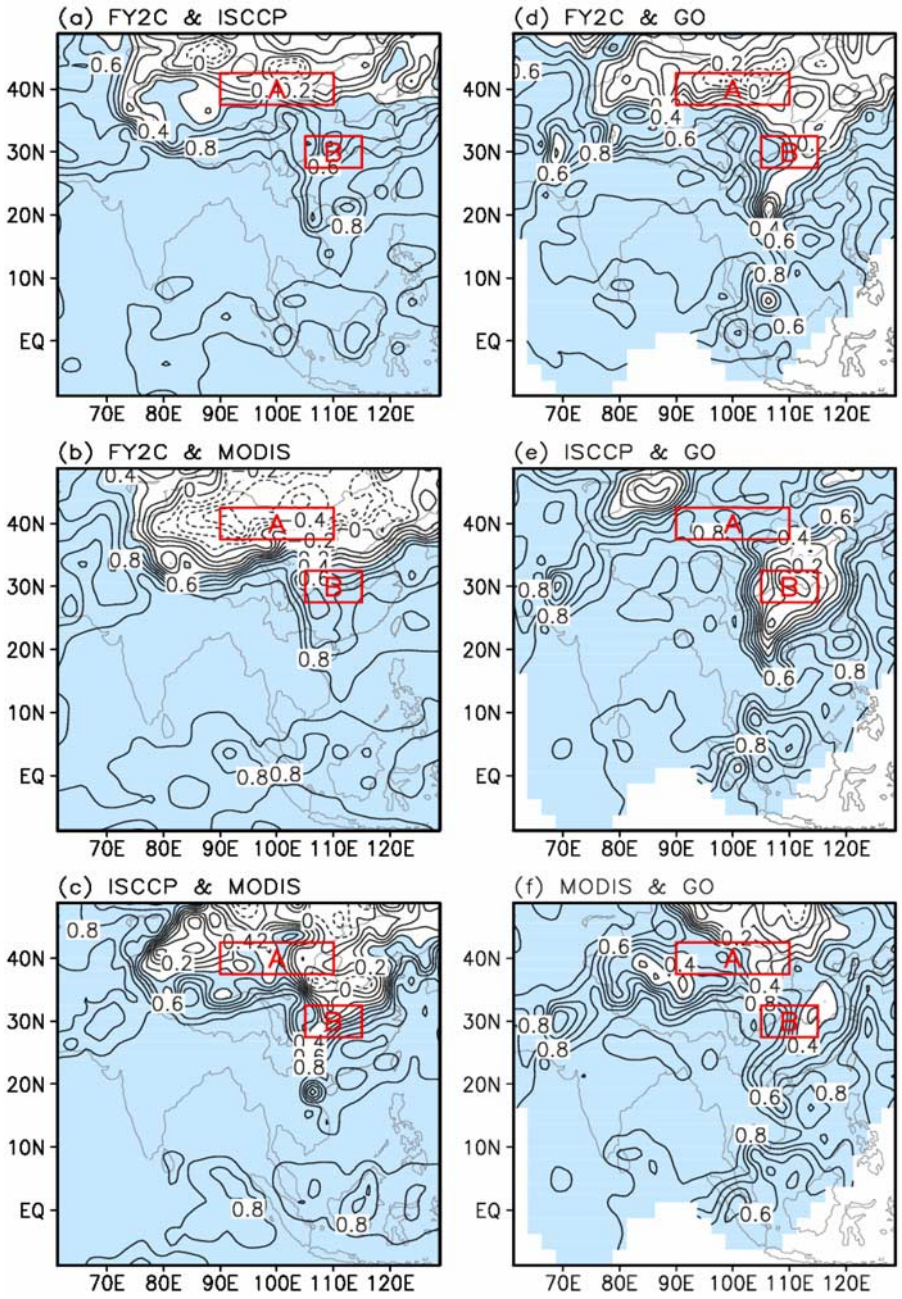

Figure 7. Temporal correlation coefficients of cloudiness between (a) FY-2C versus ISCCP, (b) FY-2C versus MODIS, (c) ISCCP versus MODIS, (d) FY-2C versus GO, (e) ISCCP versus GO, and (f) MODIS versus GO for the period from July 2005 to June 2007. Contour interval is 0.1, and the colored areas denote where the *t* test is significant at the 95% confidence level.

interrupted by a period of high cloudiness around December. This interruption is caused by the abundant cloudiness over the Chinese coastal seas in boreal winter. Over the Yangtze River valley at 30°N, high cloudiness persists for all seasons, caused by the area's particular topography and regional atmospheric circulation. GO reveals some seasonal variation with higher cloudiness in winter than in summer. This variation does not seem to be captured well by satellite observations, and ISCCP even presents an opposite seasonal cycle. MODIS seems more successful with an instrument more sensitive to low-level clouds. Around 45°N, GO and ISCCP show high cloudiness in spring and low cloudiness in autumn. FY-2C gives high cloudiness from September to November and low cloudiness from December to March. MODIS however gives high cloudiness from December to March. It is currently difficult to give a relevant explanation for these important dispersions among different data sets. The complex atmospheric circulation, together with the presence of dusts and snow cover in boreal winter, poses a main challenge for cloud detection from space.

[25] Figures 5e–5g show the differences between FY-2C and ISCCP, MODIS, and GO, respectively. In the south of

30°N, FY-2C is very close to ISCCP (Figure 5e). A small zone of negative value is observed between 20°N and 30°N, almost for the whole period. Large differences are mainly observed in the north of 30°N and have strong seasonal characteristics, with maximum positive values of about 25% from September to next January. As shown in Figure 5f, the FY-2C cloudiness is generally about 15% smaller than the MODIS cloudiness south of 30°N. North of 30°N, the main difference is again in seasonal variation: cloudiness in FY-2C is about 25% higher than that in MODIS from April to December, but slightly lower from January to March. Compared to GO (Figure 5g), FY-2C gives lower cloudiness between 15°N and 35°N, and the maximum difference occurs from November to March. North of 40°N, the FY-2C cloudiness is, however, larger than the GO cloudiness, especially from September to November.

[26] To gain more insight into the seasonal variation of cloud cover, we made another cross section following 30°N. Figure 6 shows longitude-time Hovmöller diagrams of mean cloud cover, averaged over the latitudes of 27.5°N to 32.5°N. We also plot the surface altitude at the bottom to show the influence of topography. The high-cloudiness zone in the east seems to separate from the low-cloudiness zone in the west at 103°E. FY-2C depicts clearly the high-cloudiness band at 105°E in the Sichuan Basin. This band is also present in other data sets. There is a clear seasonal cycle in MODIS and GO, but FY-2C and ISCCP fail to detect such a seasonal cycle. Midlevel cloud dominates the Sichuan Basin in general [*Yu et al.*, 2004] and is very steady, which causes difficulties for the cloud detection algorithms used in FY-2C and ISCCP. Another high-cloudiness band is at 125°E, over the East China Sea, with particularly strong values in the boreal winter. This distribution is less visible in GO, mainly because of the lack of observation stations over the ocean. Over the Tibetan Plateau from 90°E to 100°E, high cloud cover is observed from February to October and low cloud cover from November to January. West of the Tibetan Plateau, the influence of the Indian summer monsoon is clear, with high cloud cover from June to August.

3.3. Consistency of Temporal Evolution Among the Data Sets

[27] Figure 7 shows temporal correlation coefficients of monthly mean cloudiness between every pair of FY-2C, ISCCP, MODIS and GO. Satellite-derived data sets are interpolated with a bilinear scheme to individual surface stations when compared to GO (Figures 7d–7f).

[28] As shown in Figures 7a and 7b, high positive correlations for FY-2C versus ISCCP and FY-2C versus MODIS are obtained over large areas south of 30°N. The colored areas of correlation coefficients (>0.4) are where the Student's t test exceeds the 95% significance level. The strongest correlation (≥0.8) is over south Asia, where relatively smaller correlation (<0.8) is over the eastern equatorial Indian Ocean. Large positive correlations (>0.4) also exists over the western middle to high latitudes (60°E∼75°E, 30°N∼50°N). Negative or low positive correlations (<0.4) are mainly over middle and high latitudes (75°E∼130°E, 30°N∼50°N). Between FY-2C and ISCCP (Figure 7a), there is a slight negative correlation over northwestern China and southwestern Mongolia. Between

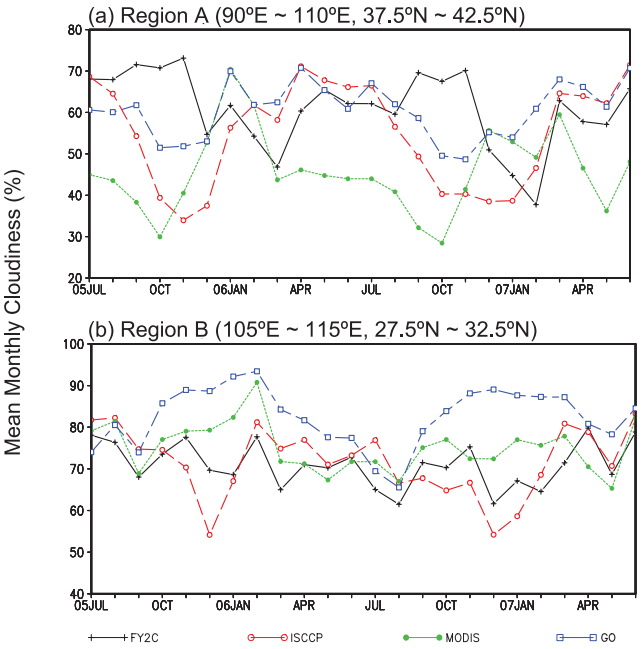

Figure 8. Regionally averaged cloudiness as a function of time from July 2005 to June 2007 for (a) region A (90°E∼110°E, 37.5°N∼42.5°N) and (b) region B (105°E∼115°E, 27.5°N∼32.5°N).

FY-2C and MODIS, the negative correlation area is obviously enlarged and spreads the whole domain of western China, northern Mongolia and northeastern China. The strongest negative correlation is larger than 0.8. The correlation between ISCCP and MODIS seems better than the correlation between others, but a weak positive correlation dominates in the same domain (Figure 7c), although small and weak negative correlations exist over Mongolia.

[29] A comparison of cloud cover derived from FY-2C with that from GO is displayed in Figure 7d. High correlation areas (>0.4) are mainly over three regions: southern Asia, southeastern Asia and the Pamir Mountains in western China. However, FY-2C has a large area of low correlation (<0.4) versus GO over northern China (Figure 7d). These two data sets are even negatively correlated over southern and eastern Mongolia, and the strongest negative value is smaller than −0.4. We also note that different areas of negative or low positive correlation features between GO and each of the two other satellite data sets occur (Figures 7e and 7f). The main low positive correlation is manifested over two major areas for ISCCP (Figure 7e): One is near the Tianshan Mountains (about 42°N and from 80°E to 90°E), and the other is over the Yangtze River valley. The cloud cover obtained from MODIS has low correlation with that from GO (Figure 7f), primarily over southern Mongolia. The strongest negative value is smaller than 0.2 in the whole studied area. In addition to the main part, the northern Tibetan Plateau and the middle reach of the Yangtze River are two other weak correlation regions.

[30] Two subareas within the study region are chosen (Figure 8) to explore the low cloudiness consistency among the four data sets. Region A (90°E∼110°E, 37.5°N∼42.5°N) represents the arid and semiarid area in northwestern China,

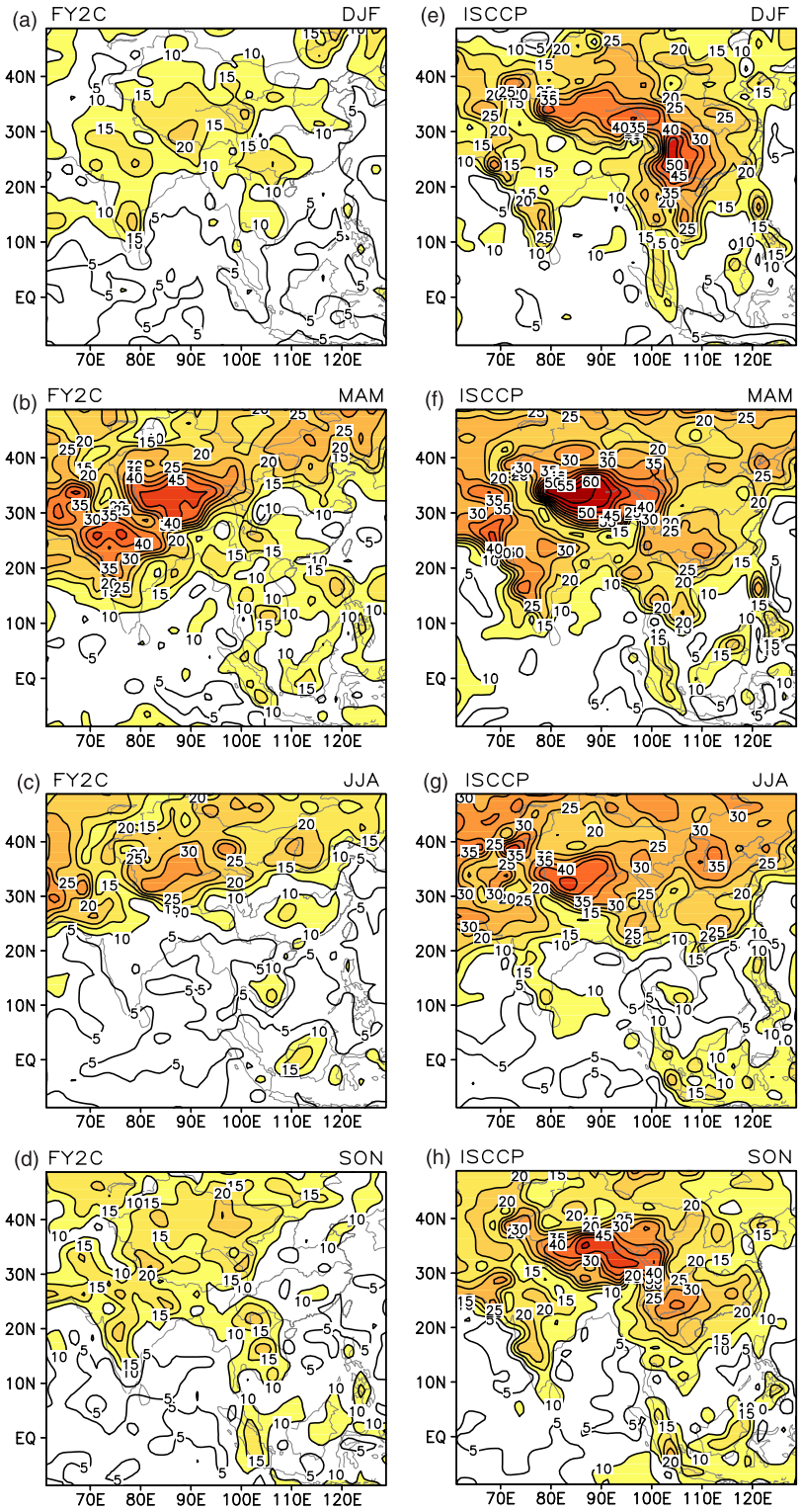

Figure 9. Cloud diurnal cycle range (% sky cover) for different seasons as depicted by (a–d) FY-2C and (e–h) ISCCP. Contour interval is 10%, and colored areas show values larger than 10%.

and region B (105°E∼115°E, 27.5°N∼32.5°N) stands for the Sichuan Basin and the middle reach of the Yangtze River valley in China.

[31] As shown in Figure 8a, there are noticeable differences between FY-2C and other data sets over region A, representing a significant antiphase. The maximum of monthly mean cloudiness from FY-2C occurs in the period from August to November, with the minimum from January to March. However, the magnitude of cloudiness obtained from MODIS is large between January and March and low

from August to November, causing the considerable negative correlation between FY-2C and MODIS (Figure 7b). The large differences over region A between different cloud data sets are possibly due to two main causes. One comes from the different cloud detection methods. The clear-sky background algorithms utilized by FY-2C and ISCCP have some difficulties in distinguishing certain types of clouds, such as nocturnal low stratus and tiny cumulus, because they lack sufficient contrast with surface radiance. The nocturnal observation of cloudiness is generally poor. Both Aqua and Terra MODIS instruments perform poorly under certain circumstances. They can misrepresent snow covered background as clouds, leading to a significant overestimation of clouds [*Z. Li et al.*, 2004; *Jin et al.*, 2007]. As shown in Figure 8a, cloudiness from MODIS is remarkably larger in winter than in other seasons. The second cause comes from different observation frequencies of the four cloud data sets. Region A is an arid and semiarid zone with a larger cloud diurnal variation (see section 3.4). It is difficult to accurately estimate the daily mean cloud fraction just with a few observations per day. Additionally, we should note that performance of satellite observations generally depends on variation of the solar zenith angle. For example, the Terra MODIS passes by southeastern Asia around 1030 local time every day and the Aqua MODIS around 1330 local time.

[32] Figure 8b depicts variation of cloud cover from the four data sets in region B. For FY-2C, seasonal variation is almost nonexistent, and the amount varies in a very small range. In contrast, GO shows noticeable seasonal variations in this region, with more clouds in winter and less in summer. ISCCP and MODIS show features quite consistent with FY-2C. Different cloud detection methods are the main causes leading to the inconsistency across data sets. Region B is a unique land region with lots of midlevel and low-level clouds [*Li et al.*, 2005]. There still remain large uncertainties for satellites to detect midlevel and low-level clouds [*Weare*, 2000]. In addition, the Sichuan Basin is a region with a very high frequency of rainfall all over the year. The clear-sky background algorithm used in FY-2C, as well as the similar algorithm used in ISCCP, has a tendency to mistakenly identify cloudy pixels as clear pixels if the pixel has been persistently covered with cloud for a long time. As shown in Figure 8b, ground-observed cloudiness is evidently higher than that of all the three satellite products. This difference could be attributed to the fact that surface observation is much more sensitive to low cloud fraction than satellite observation.

3.4. Diurnal Cycle

[33] FY-2C provides cloud cover at an interval of 1 h, which allows us to investigate the diurnal cycle of clouds. Figure 9 shows mean diurnal ranges of the FY-2C cloud cover for winter (DJF), spring (MAM), summer (JJA) and autumn (SON). The counterpart from the 3-h interval cloudiness of ISCCP D1 is also plotted in Figure 9 for comparison. We can see that the diurnal cycle of cloudiness is generally larger over land than over the ocean. The diurnal range of cloudiness over the Indian Ocean and the western Pacific is smaller than 10% sky cover. Large diurnal variation is mainly observed over the Tibetan Plateau, the northern part of the Indian Peninsula, and central Asia during boreal spring (MAM) and summer (JJA), with a maximum variation larger than 40% sky cover. For winter and autumn, the maximum diurnal range is also located over the Tibetan Plateau, Indian Peninsula and Indo-China Peninsula, with maximum values about 20% sky cover. There is a general agreement between FY-2C and ISCCP for the diurnal variation in cloudiness, but FY-2C seems to systematically estimate lower variation in the diurnal cycle.

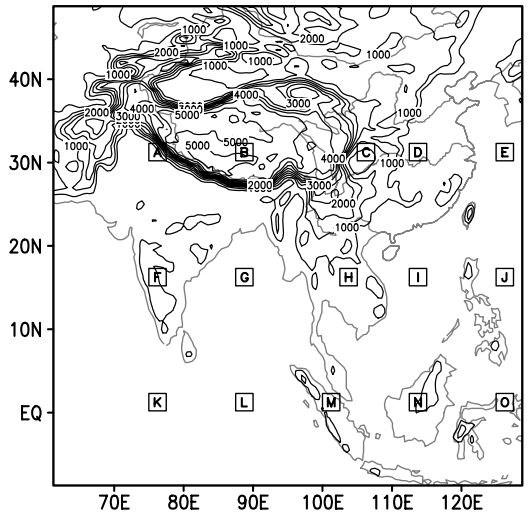

Figure 10. Surface topography (m) in Southeast Asia and the selected locations marked by letters from A to O.

[34] To go further into the cloud diurnal cycle, we selected 15 points (shown in Figure 10) along the latitudes 31.25°N, 16.25°N and 1.25°N, corresponding to the subtropical, tropical, and equatorial regions, respectively. Figure 11 gives the mean diurnal cycle of cloudiness for the four seasons separately. The locations B (31.25°N and 88.75°E) and D (31.25°N and 113.75°E) give the largest diurnal variation, in agreement with Figure 9. Again, it is generally true that the diurnal cycle over land is larger than that over the ocean. We can also observe that the peaks of the diurnal cycle are around local noon over subtropical land areas, in the morning over the Indian Peninsula, and in the afternoon near the equator (e.g., points M and N in Figure 11). Over the ocean, the diurnal variation of cloudiness is small, and it is difficult to precisely pinpoint the diurnal peaks. The diurnal variations of cloudiness over tropical and subtropical oceans are generally in agreement with the analysis of *Stubenrauch et al.* [2006].

4. Conclusions

[35] FY-2C satellite was used for the first time to investigate cloud cover in southeastern Asia. The results of a 2-year preliminary climatology study support the argument that the FY-2C cloud data set has generally a good performance compared to other cloud mask products such as ISCCP, MODIS and ground observations over southeastern Asia. FY-2C can depict the spatial distributions of cloud cover, characterized by a strong seasonal contrast. In DJF, the winter monsoon makes the whole domain dry with low cloud cover. Higher amounts of cloud can be observed over the Sichuan Basin and the East and South China Seas. Abundant cloud cover is also observed along the north-

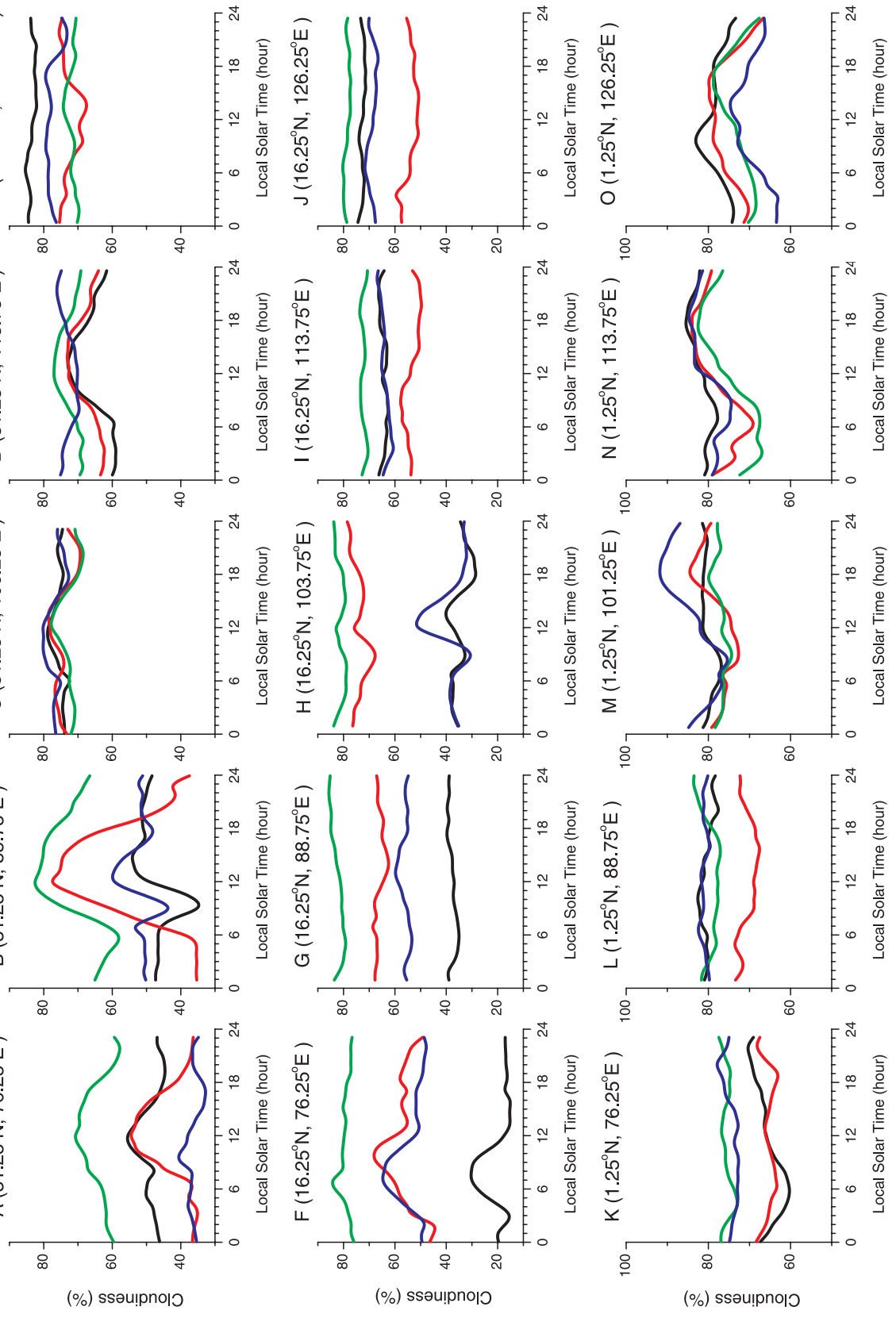

Figure 11. Diurnal variations of cloudiness (%) over different locations (shown in Figure 10) and for different seasons: winter is shown with black, spring is shown with red, summer is shown with green, and autumn is shown with blue lines. Horizontal axis is in local time.

western border of China in relation to the midlatitude jet stream instability. The ITCZ in the Southern Hemisphere is accompanied by extensive cloud cover. In JJA, the summer monsoon is the dominant system for the region of interest, which is generally humid with high levels of clouds. Those features are also exhibited by other cloud products (ISCCP, MODIS, and ground observations).

[36] Over oceans and lands at high elevation, FY-2C, MODIS and ISCCP show large differences from ground observations. This is attributed to the fact that surface observations are sparse over oceans and high lands. Over large areas in central Asia and in north China, the large discrepancies found among the four data sets are however attributed to the inefficiency of satellite cloud detection algorithms for these regions with both surface conditions and atmospheric circulations very particular. Over most areas of north China, cloud detection algorithms often operate less well over arid areas with abundant dust and higher surface albedo, and also over land covered by snow. The Sichuan Basin is another region of large discrepancies among the four cloud products, where abundant strongly steady midlevel clouds pose difficulties for the cloud detection algorithms used in FY-2C and ISCCP.

[37] The seasonal variation of cloudiness was analyzed from a latitude-time cross section over the longitudes of 105°E to 115°E and a longitude-time diagram over the latitudes of 27.5°N to 32.5°N. Large discrepancies between FY-2C cloudiness and cloudiness from ISCCP, MODIS and GO occur north of 30°N and over the Sichuan Basin. This regional inconsistency of seasonal variation is also revealed by the temporal correlation coefficients of monthly mean cloudiness between each two of FY-2C, ISCCP, MODIS and GO.

[38] The diurnal cycles of FY-2C cloudiness were analyzed for each season of the year. The diurnal range of 1-h interval cloudiness was generally larger over land than over the ocean. Large diurnal variation with a maximum larger than 40% was found mainly over the Tibetan Plateau, the northern part of the Indian Peninsula, and central Asia. These diurnal characteristics of FY-2C cloudiness generally agree with those obtained from the 3-h interval ISCCP data. But the diurnal range in FY-2C seems smaller than that in ISCCP, despite the fact that FY-2C has a more frequent sampling.

[39] FY-2 satellites (FY-2C, FY-2D and FY-2E) will extend in the future and run in a continuous manner. Further results for longer-term climatology and for a more quantitative study on the diurnal cycle of cloud cover will be reported in the future. Preliminary results on the diurnal cycle of cloudiness deduced from FY-2C seem to confirm many robust diurnal behaviors of precipitation observed in this region [*Yu et al.*, 2007; *Zhou et al.*, 2008].

[40] **Acknowledgments.** This research was partly supported by the Special Promotion Program for Meteorology (grants GYHY200806006 and GYHY(QX)2007-6-5). FY-2C data were provided by the National Satellite Meteorological Center, CMA. The ISCCP data set was downloaded from the Web site (http://isccp.giss.nasa.gov) offered by NASA Langley Research Center. MODIS data are also supplied by NASA and obtained from the MODIS Web site (http://modis.gsfc.nasa.gov/). The ground observation data set was provided by the National Meteorological Center, CMA. Comments from three anonymous reviewers were helpful for clarifying and improving the manuscript.

References

Ackerman, S. A., K. I. Strabala, W. P. Menzel, R. A. Frey, C. C. Moeller, and L. E. Gumley (1998), Discriminating clear sky from clouds with MODIS, *J. Geophys. Res.*, *103*, 32,141–32,157.

Arking, A. (1991), The radiative effects of clouds and their impact on climate, *Bull. Am. Meteorol. Soc.*, *72*, 795–813, doi:10.1175/1520-0477(1991)072<0795:TREOCA>2.0.CO;2.

Barnes, W. L., T. S. Pagano, and V. V. Salomonson (1998), Prelaunch characteristics of the Moderate Resolution Imaging Spectroradiometer (MODIS) on EOS-AM1, *IEEE Trans. Geosci. Remote Sens.*, *36*, 1088–1100, doi:10.1109/36.700993.

Barnes, W. L., V. V. Salomonson, B. Guenther, and X. Xiong (2003), Development, characterization, and performance of the EOS MODIS sensors, *Proc. SPIE Int. Soc. Opt. Eng.*, *5151*, 337–345.

Bergman, J. W., and M. L. Salby (1996), Diurnal variations of cloud cover and their relationship to climatological conditions, *J. Clim.*, *9*, 2802–2820, doi:10.1175/1520-0442(1996)009<2802:DVOCCA>2.0.CO;2.

Cairns, B. (1995), Diurnal variations of cloud from ISCCP data, *Atmos. Res.*, *37*, 133–146, doi:10.1016/0169-8095(94)00074-N.

Cess, R. D., et al. (1989), Interpretation of cloud-climate feedback as produced by 14 atmospheric general circulation models, *Science*, *245*, 513–516, doi:10.1126/science.245.4917.513.

Cox, S. K., D. S. McDougal, D. A. Randall, and R. A. Schiffer (1987), FIRE—The First ISCCP Regional Experiment, *Bull. Am. Meteorol. Soc.*, *68*, 114–118, doi:10.1175/1520-0477(1987)068<0114:FFIRE>2.0.CO;2.

Dong, X., B. Xi, and P. Minnis (2006), A climatology of midlatitude continental clouds from the ARM SGP central facility. Part II: Cloud fraction and surface radiative forcing, *J. Clim.*, *19*, 1765–1783, doi:10.1175/JCLI3710.1.

Endo, N., and T. Yasunari (2006), Changes in low cloudiness over China between 1971 and 1996, *J. Clim.*, *19*, 1204–1213, doi:10.1175/JCLI3679.1.

Hahn, C. J., W. B. Rossow, and S. G. Warren (2001), ISCCP cloud properties associated with standard cloud types identified in individual surface observations, *J. Clim.*, *14*, 11–28, doi:10.1175/1520-0442(2001)014<0011:ICPAWS>2.0.CO;2.

Hogan, R. J., C. Jakob, and A. J. Illingworth (2001), Comparison of ECMWF winter-season cloud fraction with radar-derived values, *J. Appl. Meteorol.*, *40*, 513–525, doi:10.1175/1520-0450(2001)040<0513:COEWSC>2.0.CO;2.

Hubanks, P. A., M. D. King, S. Platnick, and R. Pincus (2008), MODIS atmosphere L3 gridded product algorithm theoretical basis document, *Algorithm Theor. Basis Doc. ATBD-MOD-30*, NASA Goddard Space Flight Cent., Greenbelt, Md. (Available at http://modis-atmos.gsfc.nasa.gov/_docs/L3_ATBD_2008_12_04.pdf)

Intergovernmental Panel on Climate Change (1995), *Climate Change 1995: IPCC Second Assessment*, 572 pp., Diane, Darby, Pa.

Jin, X., J. M. Hanesiak, and D. G. Barber (2007), Time series of daily averaged cloud fractions over landfast first-year sea ice from multiple data sources, *J. Appl. Meteorol. Climatol.*, *46*, 1818–1827.

Kaiser, D. P. (1998), Analysis of total cloud amount over China, 1951–1994, *Geophys. Res. Lett.*, *25*(19), 3599–3602, doi:10.1029/98GL52784.

Kaiser, D. P. (2000), Decreasing cloudiness over China: An updated analysis examining additional variables, *Geophys. Res. Lett.*, *27*(15), 2193–2196, doi:10.1029/2000GL011358.

Klein, S. A., and D. L. Hartmann (1993), The seasonal cycle of low stratiform clouds, *J. Clim.*, *6*, 1587–1606, doi:10.1175/1520-0442(1993)006<1587:TSCOLS>2.0.CO;2.

Krüger, O., and H. Grassl (2004), Albedo reduction by absorbing aerosols over China, *Geophys. Res. Lett.*, *31*, L02108, doi:10.1029/2003GL019111.

Li, J., R. Yu, T. Zhou, and B. Wang (2005), Why is there an early spring cooling shift downstream of the Tibetan Plateau?, *J. Clim.*, *18*, 4660–4668, doi:10.1175/JCLI3568.1.

Li, Y., and H. Gu (2006), Relationship between middle stratiform clouds and large scale circulation over eastern China, *Geophys. Res. Lett.*, *33*, L09706, doi:10.1029/2005GL025615.

Li, Y., R. Yu, Y. Xu, and X. Zhang (2004), Spatial distribution and seasonal variation of cloud over China based on ISCCP data and surface observations, *J. Meteorol. Soc. Jpn.*, *82*, 761–773.

Li, Z., M. C. Cribb, F. L. Chang, and A. P. Trishchenko (2004), Validation of MODIS-retrieved cloud fractions using wholesky imager measurements at the three ARM sites, paper presented at 14th ARM Science Team Meeting, U.S. Dep. of Energy, Albuquerque, N. M. (Available at http://www.arm.gov/publications/proceedings/conf14/extended_abs/li1-z.pdf)

Liou, K. N. (1986), Influence of cirrus clouds on weather and climate: A global perspective, *Mon. Weather Rev.*, *114*, 1167–1199, doi:10.1175/1520-0493(1986)114<1167:IOCCOW>2.0.CO;2.

Lu, F., X. Zhang, and J. Xu (2008), Image navigation for the FY2 geosynchronous meteorological satellite, *J. Atmos. Oceanic Technol.*, *25*, 1149–1165, doi:10.1175/2007JTECHA964.1.

Mace, G. G., and S. Benson (2008), The vertical structure of cloud occurrence and radiative forcing at the SGP ARM site as revealed by 8 years of continuous data, *J. Clim.*, *21*, 2591–2610, doi:10.1175/2007JCLI1987.1.

Menzel, W. P., R. A. Frey, H. Zhang, D. P. Wylie, C. C. Moeller, R. E. Holz, B. Maddux, B. A. Baum, K. I. Strabala, and L. E. Gumley (2008), MODIS global cloud-top pressure and amount estimation: Algorithm description and results, *J. Appl. Meteorol. Climatol.*, *47*, 1175–1198, doi:10.1175/2007JAMC1705.1.

Mokhov, I. I., and M. E. Schlesinger (1994), Analysis of global cloud amount, *J. Geophys. Res.*, *99*, 17,045–17,065, doi:10.1029/94JD00943.

Pavolonis, M. J., and J. R. Key (2003), Antarctic cloud radiative forcing at the surface estimated from the AVHRR Polar Pathfinder and ISCCP D1 datasets, 1985–93, *J. Appl. Meteorol.*, *42*, 827–840, doi:10.1175/1520-0450(2003)042<0827:ACRFAT>2.0.CO;2.

Qian, Y., D. P. Kaiser, L. R. Leung, and M. Xu (2006), More frequent cloud-free sky and less surface solar radiation in China from 1955 to 2000, *Geophys. Res. Lett.*, *33*, L01812, doi:10.1029/2005GL024586.

Ramanathan, V., R. D. Cess, E. F. Harrison, P. Minnis, B. R. Barkstorm, and D. Hartman (1989), Cloud radiative forcing and climate: Results from the Earth Radiation Budget Experiment, *Science*, *243*, 57–63, doi:10.1126/science.243.4887.57.

Rossow, W. B., and L. C. Garder (1993a), Cloud detection using satellite measurements of infrared and visible radiances for ISCCP, *J. Clim.*, *6*, 2341–2369, doi:10.1175/1520-0442(1993)006<2341:CDUSMO>2.0.CO;2.

Rossow, W. B., and L. C. Garder (1993b), Validation of ISCCP cloud detections, *J. Clim.*, *6*, 2370–2393, doi:10.1175/1520-0442(1993)006<2370:VOICD>2.0.CO;2.

Rossow, W. B., and A. A. Lacis (1990), Global, seasonal cloud variations from satellite radiance measurements. Part II: Cloud properties and radiative effects, *J. Clim.*, *3*, 1204–1253, doi:10.1175/1520-0442(1990)003<1204:GSCVFS>2.0.CO;2.

Rossow, W. B., and R. A. Schiffer (1999), Advances in understanding clouds from ISCCP, *Bull. Am. Meteorol. Soc.*, *80*, 2261–2287, doi:10.1175/1520-0477(1999)080<2261:AIUCFI>2.0.CO;2.

Rossow, W. B., and Y.-C. Zhang (1995), Calculation of surface and top-of-atmosphere radiative fluxes from physical quantities based on ISCCP datasets: 2. Validation and first results, *J. Geophys. Res.*, *100*, 1167–1197, doi:10.1029/94JD02746.

Salomonson, V. V., W. L. Barnes, P. W. Maymon, H. E. Montgomery, and H. Ostrow (1989), MODIS: Advanced facility instrument for studies of the Earth as a system, *IEEE Trans. Geosci. Remote Sens.*, *27*, 145–153, doi:10.1109/36.20292.

Stephens, G. L. (2005), Cloud feedbacks in the climate system: A critical review, *J. Clim.*, *18*, 237–273, doi:10.1175/JCLI-3243.1.

Stephens, G. L., and T. J. Greenwald (1991), The Earth's radiation budget and its relation to atmospheric hydrology: 2. Observations of cloud effects, *J. Geophys. Res.*, *96*(D8), 15,325–15,340, doi:10.1029/91JD00972.

Stephens, G. L., and C. D. Kummerow (2007), The remote sensing of clouds and precipitation from space: A review, *J. Atmos. Sci.*, *64*(11), 3742–3765, doi:10.1175/2006JAS2375.1.

Stubenrauch, C. J., A. Chédin, G. Rädel, N. A. Scott, and S. Serrar (2006), Cloud properties and their seasonal and diurnal variability from TOVS Path-B, *J. Clim.*, *19*, 5531–5553, doi:10.1175/JCLI3929.1.

Wang, W. C., W. Gong, W. S. Kau, C. T. Chen, H. H. Hsu, and C. H. Tu (2004), Characteristics of cloud radiative forcing over east China, *J. Clim.*, *17*, 845–853, doi:10.1175/1520-0442(2004)017<0845:COCRFO>2.0.CO;2.

Warren, S. G., R. M. Eastman, and C. J. Hahn (2007), A survey of changes in cloud cover and cloud types over land from surface observations, 1971–96, *J. Clim.*, *20*, 717–738, doi:10.1175/JCLI4031.1.

Weare, B. C. (2000), Near-global observations of low clouds, *J. Clim.*, *13*, 1255–1268, doi:10.1175/1520-0442(2000)013<1255:NGOOLC>2.0.CO;2.

World Meteorological Organization (1975), *International Cloud Atlas: Manual on the Observation of Clouds and Other Meteors*, vol. I, *WMO Ser.*, vol. 407, Geneva.

World Meteorological Organization (1987), *International Cloud Atlas*, vol. II, *WMO Ser.*, vol. 407, Geneva.

Wylie, D. P., and H. M. Woolf (2002), The diurnal cycle of upper tropospheric clouds measured by GOES-VAS and the ISCCP, *Mon. Weather Rev.*, *130*, 171–179, doi:10.1175/1520-0493(2002)130<0171:TDCOUT>2.0.CO;2.

Xu, J., F. Lu, and Q. Zhang (2002), Automatic navigation of FY-2 geosynchronous meteorological satellite images, paper presented at the 6th International Winds Workshop, EUMETSAT, Madison, Wis.

Yang, C., J. Xu, and F. Zhao (2008), Application of time series in FY2C cloud detection (in Chinese), *J. Atmos. Environ. Opt.*, *3*, 377–391.

Yu, R., B. Wang, and T. Zhou (2004), Climate effects of the deep continental stratus clouds generated by Tibetan Plateau, *J. Clim.*, *17*, 2702–2713, doi:10.1175/1520-0442(2004)017<2702:CEOTDC>2.0.CO;2.

Yu, R., T. Zhou, A. Xiong, Y. Zhu, and J. Li (2007), Diurnal variations of summer precipitation over contiguous China, *Geophys. Res. Lett.*, *34*, L01704, doi:10.1029/2006GL028129.

Zhang, W., J. Xu, C. Dong, and J. Yang (2006), China's current and future meteorological satellite systems, in *Earth Science Satellite Remote Sensing*, vol. 1, *Science and Instruments*, edited by J. J. Qu et al., pp. 392–413, doi:10.1007/978-3-540-37293-6_20, Tsinghua Univ. Press, Beijing.

Zhou, T., R. Yu, H. Chen, A. Dai, and Y. Pan (2008), Summer precipitation frequency, intensity, and diurnal cycle over China: A comparison of satellite data with rain gauge observations, *J. Clim.*, *21*, 3997–4010, doi:10.1175/2008JCLI2028.1.

X. Jin, L. Li, and T. Wu, National Climate Center, China Meteorological Administration, 46 Zhongguancun Nandajie, Beijing 100081, China. (twwu@cma.gov.cn)

C. Shi, National Satellite Meteorological Center, China Meteorological Administration, Beijing 100081, China.